



OPEN

Evaluation of transmission characteristics of CVD-grown graphene and effect of tuning electrical properties of graphene up to 50 GHz

Ryota Okuda^{1,2✉}, Kazuhiko Niwano¹, Kaname Hatada², Kei Kokubu², Ryosuke Suga², Takeshi Watanabe² & Shinji Koh²

Graphene has been investigated as a transparent conductive film for use in a variety of devices, and in recent years it has shown promise for use in millimeter-wave devices as 5G technology. In this study, we applied single-layer (SL), triple-layer (3L), and P-type doped 3L graphene to coplanar waveguide (CPW) transmission lines and obtained transmission characteristics (S_{21}) from 1 to 50 GHz, which covered the 5G band. Furthermore, an equivalent circuit model of the CPW used in the measurements was constructed and simulations were performed, which showed good agreement with the measured results. The results validated the transmission properties of the graphene and the contact impedance at the interface between electrodes and the graphene in CPW circuits, which are necessary parameters for designing antennas using graphene. In addition, by comparing the transmission loss of three types of graphene, the parameters for improving the transmission characteristics were clarified.

In recent years, various conductive materials have been considered for applications of millimeter-wave device as fifth generation (5G) technology^{1–3}. In particular, transparent conductive materials are attracting attention because they can be installed in a variety of locations without compromising their appearance. For example, indium tin oxide⁴, indium zinc tin oxide⁵, and meshed Cu formed on a substrate⁶ are commonly used, however, these materials have drawbacks such as trade-offs between electrical resistance and optical transparency^{7,8}. Since our previous report, we have been focusing on chemical vapor deposition (CVD) grown graphene^{9,10}. In general, graphene has excellent optical transparency and can be transferred onto various shapes and types of substrates due to its robustness and flexibility. If graphene can be implemented as a transparent 5G antenna, it can be embedded in transparent objects that require high optical transparency, such as building windows, car windshields, and mobile phones. However, graphene has higher carrier mobility but lower carrier concentration than metals, resulting in higher electrical resistance. This poses a challenge for its application in millimeter-wave devices. Recently, graphene has been extensively studied as an alternative material to metals, and various studies have been conducted to achieve low resistance while maintaining transparency using methods such as multilayering^{11,12} and carrier doping^{13,14}. There have been reports investigating the electrical properties of graphene itself and its application to millimeter-wave devices. Pan et al. fabricated the slot antennas using ink containing graphene and evaluated their radiation characteristics up to 18 GHz¹⁵. Sadon et al. reported printed array antennas with graphene and their radiation characteristics and beamforming capability at 15 GHz¹⁶. Hong et al. compared the electromagnetic interference (EMI) shielding performance of graphene with different qualities by changing the CVD process parameters¹⁷. On the other hand, there are limited reports evaluating the characteristics of devices using various types of graphene with different electrical properties in the frequency bands used for 5G technology (24.5 to 27.5 GHz and 37.0 to 43.5 GHz). Zhang et al. have evaluated transmission properties up to 40 GHz by applying graphene to a coplanar waveguide (CPW) with different structures with single layer graphene¹⁸. Similarly, Moon et al. evaluated the transmission properties of graphene from 0.5–110 GHz with different number of layers¹⁹. Grande et al. evaluated microwave ring resonators with multilayering and SOCl₂

¹Technology General Division, Materials Integration Laboratories, AGC Inc., Yokohama 230-0045, Japan. ²Department of Electrical Engineering and Electronics, College of Science and Engineering, Aoyama Gakuin University, Sagami-hara 252-5258, Japan. ✉email: Ryota.okuda@agc.com

doping up to 10 GHz²⁰. While device applications of graphene in the terahertz band^{21–23} have attracted much attention, there is insufficient research targeting the millimeter-wave region for 5G applications, which we aim to cover in our study.

In this report, we systematically evaluate the effects of graphene multilayering and carrier doping on transmission characteristics (S_{21}) from 1 to 50 GHz. Three types of graphene were fabricated: single-layer (SL), three-layer (3L), and P-type carrier doped 3L graphene with TFSA (Bis (trifluoromethanesulfonyl) amide) as the dopant, and their S_{21} were measured. Furthermore, the electrical properties of graphene in the CPW were clarified by simulating the S_{21} using the constructed equivalent circuit model of the CPW and comparing it with the measured S_{21} of the CPW. The results clarified the behavior of three types of graphene in millimeter-wave devices such as its transmission characteristics and contact characteristics at the interfaces between graphene and electrodes, which are necessary parameter for designing antennas using graphene.

Results and discussions

In our study, SL, 3L, and P-type doped 3L graphene were fabricated to clarify how the transmission properties of graphene change with the number of layers and carrier doping. The fabrication of graphene and the devices for evaluation are described in the “Methods” section.

Optical transmittance in visible region. The optical transmittances in the visible region of the SL, 3L, and P-type doped graphene are shown in Fig. 1. Because a certain area ($2 \times 7 \text{ mm}^2$) is required to evaluate optical transmittance evaluation, three types of graphene ($10 \times 10 \text{ mm}^2$) were transferred to a quartz substrate and evaluated optical properties before forming the device. Furthermore, carrier doping was performed on 3L graphene before device fabrication, and the optical transmittance of P-type doped 3L graphene was evaluated. Note that the optical transmittance of the quartz substrate was subtracted for reference to discuss the optical properties of graphene only. As shown in Fig. 1, SL graphene showed the highest transmittance (97% at 500 nm). Graphene has an absorption of about 2.3% per layer in a visible wavelength region. Therefore, the transmittance of 3L graphene (89% at 500 nm) was lower than that of the SL graphene. Notably, P-type doped 3L graphene exhibited an optical transparency similar to pristine 3L graphene (90% at 500 nm). The P-type doping has the effect of increasing carrier density because it adds more holes, which is expected to improve conductivity²⁴. Being able to improve electrical conductivity while maintaining optical transparency is a unique feature of graphene.

Raman spectra of graphene. The Raman spectra of the three types of graphene are shown in Fig. 2. The measurements were performed at the center of the graphene channels of the CPW devices. After evaluating the Raman spectra of 3L graphene, carrier doping was performed on the same sample to obtain the Raman spectra of P-type doped 3L graphene. G peaks at $1580\text{--}1600 \text{ cm}^{-1}$ and 2D peaks at $2680\text{--}2700 \text{ cm}^{-1}$, which are characteristic of graphene, were observed as shown in Fig. 2a. For all samples, slight D peaks were observed at $1360\text{--}1370 \text{ cm}^{-1}$, which may be due to the defects induced during the transferring, stacking and fabricating the CPW processes. Significant damage was not observed with the optical microscope observation in Fig. S1. The intensity ratio of the 2D peak to the G peak in the Raman spectra (I_{2D}/I_G) correlate with the stacking structure of a multilayer graphene. The obtained I_{2D}/I_G of the 3L graphene was 1.5, which is as high as that of SL graphene ($I_{2D}/I_G = 1.5$). As shown in Fig. 2a, the full width at half maximum (FWHM_{2D}) from fitting the 2D peak with the Lawrence function indicates that 3L graphene ($\text{FWHM}_{2D}:35.2$) is close to SL graphene ($\text{FWHM}_{2D}:35.1$). These suggested 3L graphene had a turbostratic stacking structure, which is characteristic of multilayer graphene obtained from a layer-by-layer process using polycrystalline graphene grown on polycrystalline Cu foils^{10,18,25}. In general, the G peak of graphene originates from the in-plane motion of carbon atoms and shifts toward higher

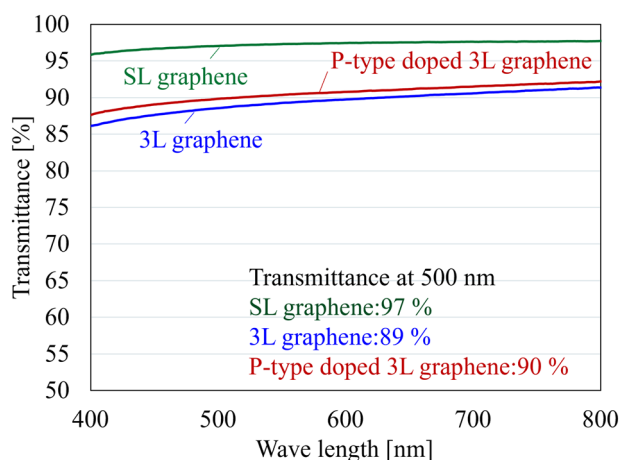


Figure 1. Visible spectral evaluation of SL graphene (green), 3L graphene (blue) and P-type doped 3L graphene (red).

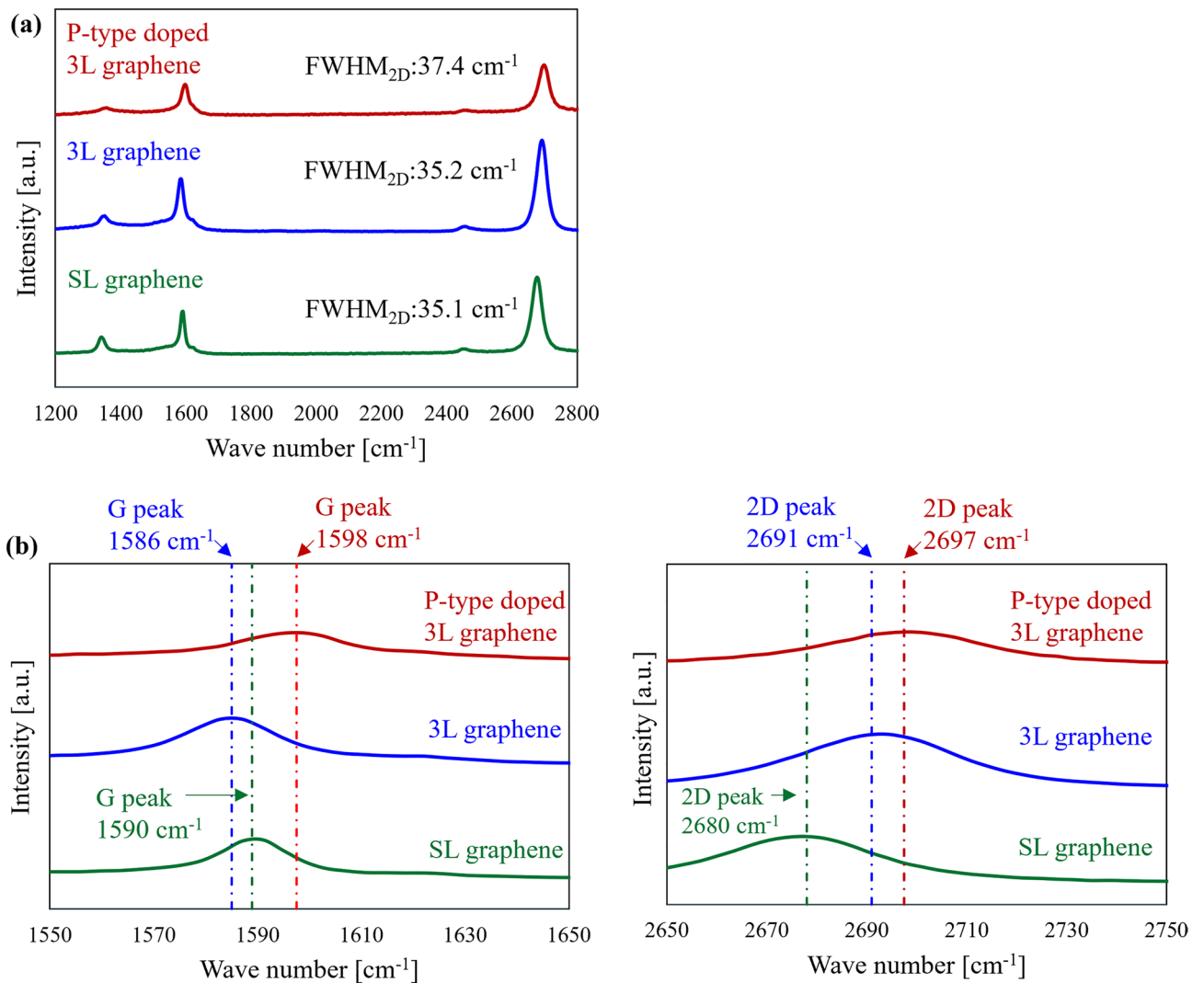


Figure 2. (a) Raman spectra of SL graphene (green), 3L graphene (blue) and P-type doped 3L graphene (red) (b) Raman shift of SL graphene, 3L graphene and P-type doped 3L graphene of G and 2D peaks.

energies with higher carrier density^{26,27}. In Fig. 2b, the G peak of 3L graphene was observed to shift from 1583 to 1598 cm^{-1} , which supported P-type doping with TFSA.

Characterization of transmission characteristics (S_{21}) using CPW devices. CPWs were used to evaluate the S_{21} of graphene (Fig. 3a). A CPW consists of a signal line and ground lines and can be mounted on only one side of the board. Therefore, it is suitable for graphene evaluation because three-terminal probe measurements can be easily performed. CPWs with three types of graphene were fabricated by depositing Au as an electrode on the graphene samples and performing lithography. The characteristic impedance of the signal and ground lines was designed to have a characteristic impedance of 50 Ω ²⁸, with a signal line width of 400 μm and gaps of 36 μm between the signal line and ground lines. The graphene channel was formed to be 30 \times 400 μm^2 (Fig. 3a,b). Note that graphene is under each of the signal and ground lines with Au. The S_{21} of the fabricated CPW was measured from 1 to 50 GHz using a microwave probe (Form Factor, |Z| Probe GSG 500 μm) with guaranteed measurement range from DC to 50 GHz, a probe station (Form Factor, PM8), and a vector network analyzer (Keysight Technologies, E8361A) as shown in Fig. 3c,d. For the S_{21} measurement, the CPW was connected to two ports of the vector network analyzer and input impedance of 50 Ω was extracted. After calibrating shorts, opens, loads, and throughs, the S_{21} was measured.

Equivalent circuit model of CPW. To analyze the contact impedance and the transmission characteristics of the graphene samples, an equivalent circuit model of the CPW was constructed as shown in Fig. 4^{29,30}. The contact impedance between graphene and Au in the CPW transmission line was treated as a parallel circuit of contact resistance R_{contact} and contact capacitance C_{contact} . To prevent delamination of the Au electrodes in the probe measurement, the probe was contacted about 200 μm inside from both ends of the transmission line. For the frequency from 1 to 50 GHz, the areas between the probe contact position and the edge of the transmission

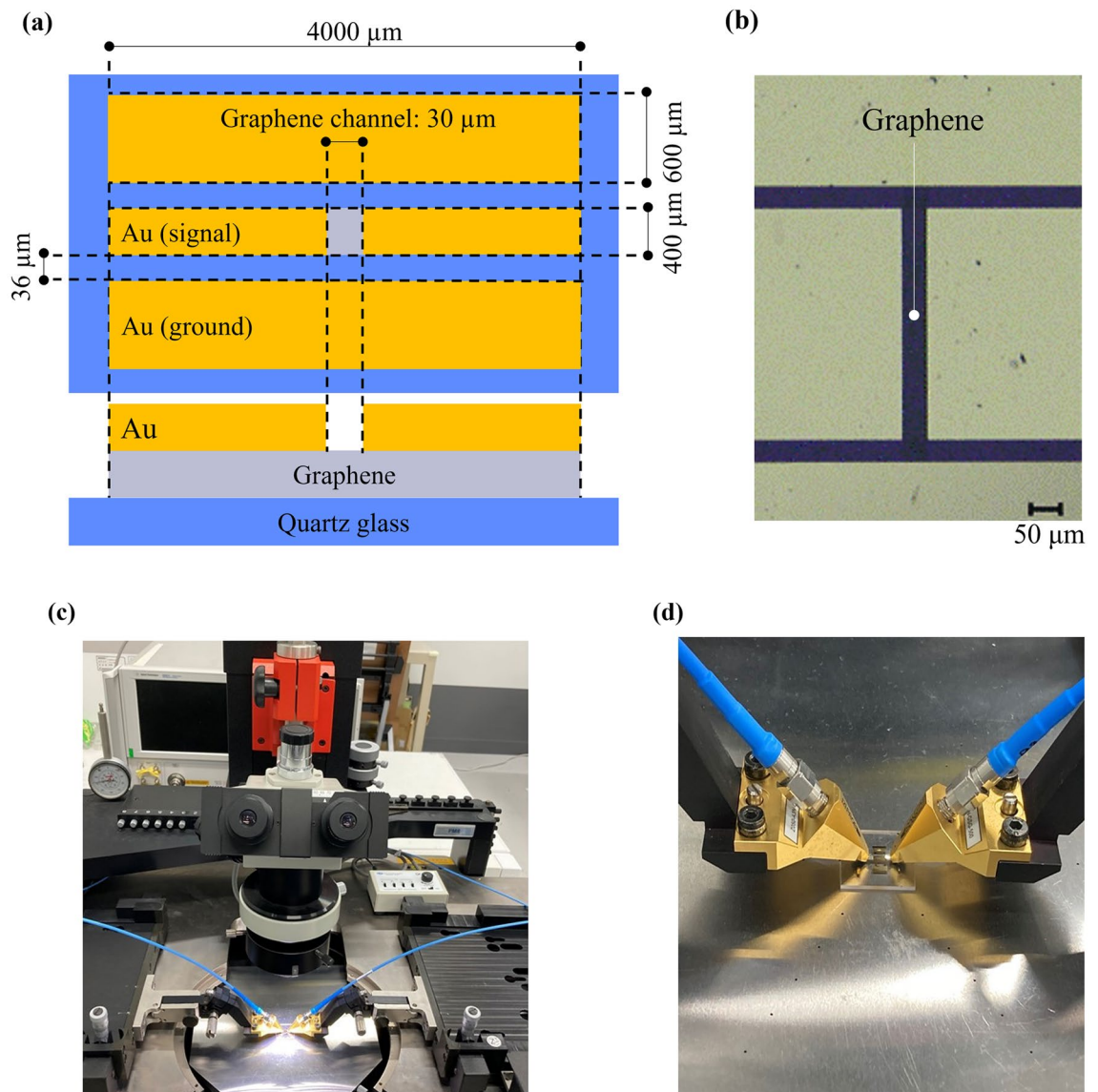


Figure 3. (a) Design and (b) optical microscope image of CPW. (c) Measurement system. (d) Probe measurement area.

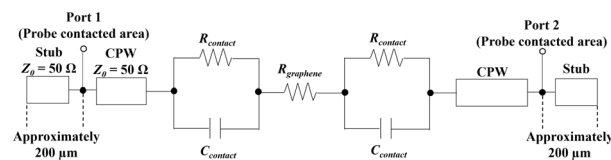


Figure 4. Equivalent circuit model of CPW.

line could act as an open stub, so the distance between the probe contacted area and the end of the transmission line was incorporated into the equivalent circuit as a transmission line with a characteristic impedance of 50 Ω (Fig. S2).

The graphene channel in the transmission line was expressed only in terms of frequency-independent impedance as $R_{graphene}$. In the Drude model, the conductivity of graphene must take into account the frequency dependence associated with carrier scattering. This scattering follows an exponential relaxation time τ (0.01–2 picoseconds) depending on the mobility, Fermi level, and Fermi velocity^{31,32}. The characteristic exponential relaxation time of $\tau = 2$ picoseconds corresponds to $\omega/2\pi = 5.0 \times 10^{11}$ (500 GHz), which means that the resistor–capacitor (RC) network can be considered constant at least up to 500 GHz^{33,34}. Furthermore, the skin effect of the conductor

is also frequency dependent. The thickness of the skin effect from typical CVD graphene conductivity (1.0×10^6 S/m) is 2.3–16 μm ³⁵ from 1 to 50 GHz as calculated using the following equation,

$$d = \sqrt{\frac{2\rho}{\omega\mu}} [m]$$

which is much thicker than 3L graphene, and the equivalent circuit model was constructed assuming that the frequency dependence of the impedance of the graphene channel in transmission line is negligible³⁶. In parallel with R_{graphene} , the parasitic capacitance generation between Au electrodes across graphene channel can also be accounted for, but it was not included in the equivalent circuit model because the electrode thickness (500 nm) is thin and the distance between electrodes across graphene channels (30 μm) in Fig. 3a is presumed to be greater than the distance between Au and graphene.

To assign the impedance such as R_{contact} and R_{graphene} of the equivalent circuit model (Fig. 4), experimental measurements were conducted using three types of graphene.

Impedance of R_{graphene} . To determine R_{graphene} , Hall effect measurements were performed on the three types of graphene using the van der Pauw method (Fig. 5a). Such properties can be measured without effects from the contact resistance. The results of the Hall effect measurements (Fig. 5b) are shown in Table 1. The carrier mobility of 3L graphene (2250 cm^2/Vs) improved compared to that of SL graphene (1200 cm^2/Vs). This suggests that graphene is less likely to be affected by carrier scattering effects from the quartz substrate due to multilayering³⁷. The sheet resistance of graphene (R_{sheet}) was 758 Ω , 405 Ω , and 125 Ω for SL, 3L, and P-type doped 3L graphene, respectively. The carrier mobility (1090 cm^2/Vs) of P-type doped 3L graphene decreased with TFSA doping, while the sheet resistance decreased with high carrier density ($4.6 \times 10^{13} \text{ cm}^{-2}$). A comparison of the carrier mobility of SL graphene ($4.6 \times 10^{12} \text{ cm}^{-2}$) and 3L graphene ($6.8 \times 10^{12} \text{ cm}^{-2}$) shows that carrier doping is effective in lowering resistivity. R_{graphene} in the transmission line was determined from R_{sheet} taking into account the shape of the signal line of the CPW (Fig. 3a) as follows

$$R_{\text{graphene}} = R_{\text{sheet}} \times \left(\frac{L}{W} \right)$$

where W is the length (30 μm) and L is the width of the graphene channel in the transmission line (Fig. 3a). As shown in Table 1, the determined R_{graphene} values were lowest for P-type doped 3L graphene (13 Ω) versus SL (42 Ω) and 3L graphene (78 Ω).

Contact resistance R_{contact} . To obtain R_{contact} between graphene and Au electrode, the transfer length method (TLM) was utilized as shown in Fig. 6. In the TLM results, the Y-axis intercept refers to $2R_{\text{TLM}}$ between

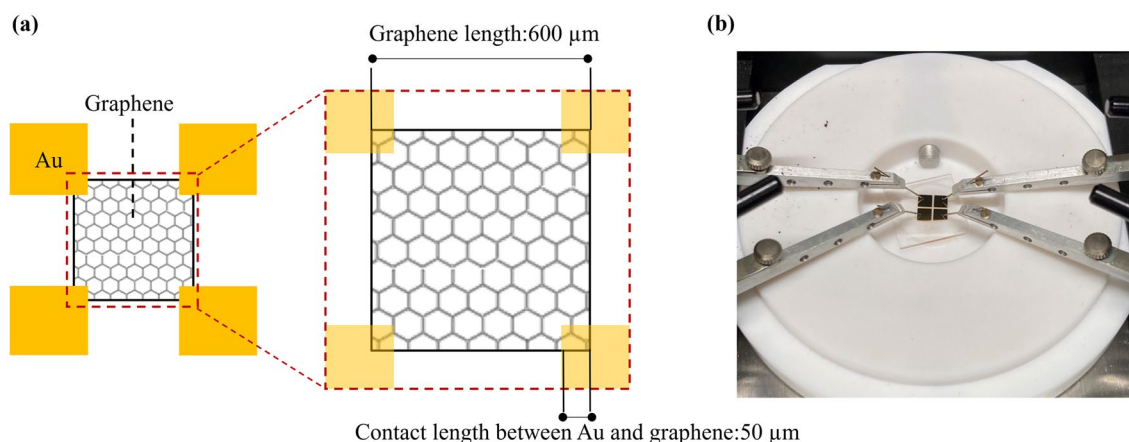


Figure 5. (a) Design and (b) image of Hall effect measurement.

	SL graphene	3L graphene	P-type doped 3L graphene
R_{sheet} [Ω]	758	405	125
Carrier mobility [cm^2/Vs]	1200	2250	1090
Carrier density [$1/\text{cm}^2$]	4.6×10^{12}	6.8×10^{12}	4.6×10^{13}
R_{graphene} [Ω]	78	42	13

Table 1. Results of Hall effect measurement of three types of graphene.

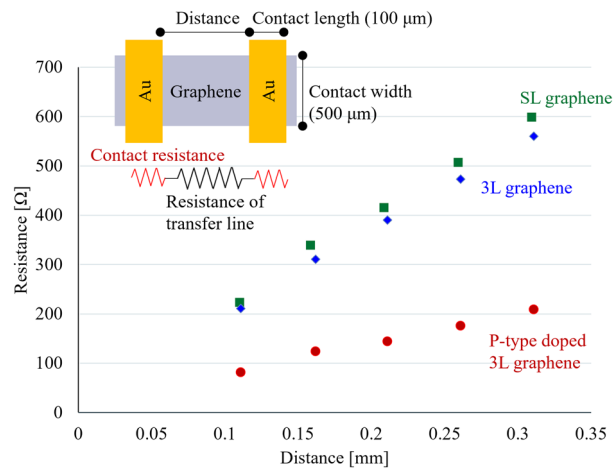


Figure 6. TLM for three types of graphene.

Au and the graphene^{38–40}. The value of R_{contact} was determined from the contact width between graphene and Au electrode (500 μm ; Fig. 6) and the width between graphene and the Au electrode in the CPW (400 μm ; Fig. 3a) as shown in Table 2. Kosuga et al. reported an R_{contact} of 50 Ω for SL graphene using TLM²⁸, which is not significantly different from our data (Table 2). The X-axis intercept of the straight lines in Fig. 6 represents the effective length (L_t) that contributed to the contact between the Au electrode and graphene. S_t between the graphene and Au electrodes in the CPW circuit can be expressed as

$$S_t = L_t \times W$$

Where W is the width of the CPW signal line (400 μm). P-type doped 3L graphene exhibited an increase in S_t with P-type doping ($5.3 \times 10^{-5} \text{ cm}^2$) as shown in Table 2. This is based on the increase in the density of states (DOS) due to the lowering of the Fermi level, and as a result, P-type doped 3L graphene exhibited the lowest R_{contact} value.

Contact capacitance C_{contact} . C_{contact} can be treated as a series circuit of the quantum capacitance of graphene (C_q) and the geometrical capacitance (C_g) between Au and graphene.

$$C_{\text{contact}} = \left(\frac{1}{C_q} + \frac{1}{C_g} \right)^{-1} \text{ [F]}$$

C_q and C_g can be obtained as follows^{41–43},

$$C_q = \frac{2e^2 E_F}{\pi (v_F \hbar)^2} \times S_t' \text{ [F]}$$

$$C_g = \frac{\epsilon}{d} \times S_t' \text{ [F]}$$

where E_F is the Fermi energy, v_F is the Fermi velocity ($1 \times 10^8 \text{ cm/s}$), \hbar is the reduced Planck's constant, and S_t' is the effective contact area between graphene and Au in the AC circuit. ϵ is the dielectric constant, and d corresponds to the distance between the electrode and graphene. Here, in the DC circuit, the effective contact area between graphene and Au (S_t) can be obtained from the TLM measurement. However, S_t' in the high-frequency band is difficult to determine because the current distributions in the CPW differ from that in DC measurements

	SL graphene	3L graphene	P-type doped 3L graphene
R_{TLM} [Ω]	16	12	8
R_{contact} [Ω]	20	15	10
S_t [cm^2]	3.4×10^{-5}	2.8×10^{-5}	5.3×10^{-5}

Table 2. R_{contact} of three types of graphene obtained from TLM measurements.

due to the current crowding and its frequency dependence. Therefore, $C_{contact}$ was treated as a fitting parameter in the analysis of S_{21} , in which the measured S_{21} is compared to the simulations.

Evaluation of S_{21} . The electrical properties of the three types of graphene were reflected in an equivalent circuit model (Fig. 4) to simulate the S_{21} . The simulations were performed using a 3D planar high-frequency electromagnetic software (Sonnet Lite 18.53), and after fitting $C_{contact}$ (Fig. S3), the transmission characteristics of graphene were evaluated by comparing them with the measured results. The $C_{contact}$ fitting was performed as shown in Fig. S3. The impedance of capacitance is shown below.

$$Z = \left| \frac{1}{2\pi f C_{contact}} \right|$$

where f corresponds to frequency. The $C_{contact}$ fitting was performed at lower frequencies because $C_{contact}$ has a greater effect on contact impedance becomes large when the frequency is close to 1 GHz. Fig. S3 shows that the S_{21} calculation results were close to the measured values and saturated when the $C_{contact}$ is above 200 pF for SL and 3L graphene and above 1 nF for P-type doped 3L graphene. From the results, the value of $C_{contact}$ of three types of graphene could not be uniquely determined. Therefore, for the S_{21} calculations, the $C_{contact}$ of SL and 3L graphene was regarded as 200 pF and the $C_{contact}$ of P-type doped 3L graphene was treated as 1 nF. Our findings suggest that the larger $C_{contact}$ of P-type doped 3L graphene is due to the increase in quantum capacitance (C_q) resulting from the increase in carrier density (Table 1). Hence, the value of $C_{contact}$ may have changed as the value of C_q increased. This indicates that the values of C_q and C_g are comparable.

Figure 7a shows the magnitude of S_{21} versus frequency. Comparing the magnitudes of the three types of graphene, the transmission loss decreased in the order of SL, 3L, and P-type doped 3L graphene. The transmission loss was smaller with lower values of the $R_{graphene}$ in the graphene channel (Fig. 3a), indicating that the multilayering and carrier doping of graphene are effective for reducing the transmission loss.

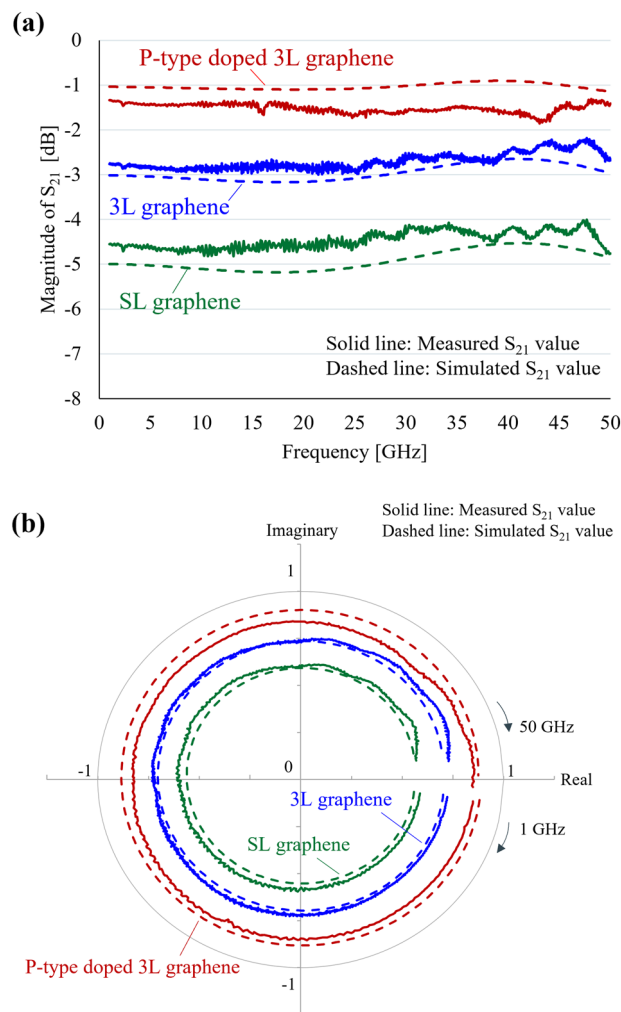


Figure 7. Measured (solid line) and calculated (dashed line) S_{21} for SL graphene (green), 3L graphene (blue), and P-type 3L graphene (red) from 1 to 50 GHz. (a) Magnitude of S_{21} for frequency. (b) Polar chart.

Figure 7b shows the experimental and calculated results of the S_{21} of the CPW in a polar chart. The polar coordinates represent the *Real* part on the X-axis and the *Imaginary* part on the Y-axis, and can be obtained from the magnitude and phase of S_{21} by the following equation. Hence, the phase and magnitude can be compared from the polar chart.

$$Real = 10^{(Magnitude[dB]/20)} \times \cos\left(\frac{phase[deg.] \times \pi}{180[deg.]}\right)$$

$$Imaginary = 10^{(Magnitude[dB]/20)} \times \sin\left(\frac{phase[deg.] \times \pi}{180[deg.]}\right)$$

Because the maximum value of magnitude is 0 dB, the X and Y-axes of the polar chart take values from -1 to 1. Here, magnitude and phase can be converted using the following equation.

$$Magnitude [dB] = 20\log_{10}\sqrt{Real^2 + Imaginary^2}$$

$$Phase [deg.] = \text{Arctangent}\left(\frac{Imaginary}{Real}\right)$$

The magnitude increases when the *Real* and *Imaginary* parts are large. In other words, when the value of *Real* and *Imaginary* are far from the origin in the polar chart, it means that the transmission loss is small. As shown in Fig. 7b, for both graphene samples, the calculated and experimental values were in close agreement from 1 to 50 GHz. These results indicate that both the magnitude and the phase were accurate, thus validating the design policy of this equivalent circuit model. Furthermore, the results indicate that the impedance of graphene channel in the CPW (Fig. 3a) can be expressed only in terms of resistance from 1 to 50 GHz frequency, as discussed in the previous section. It is also demonstrated that the introduction of open stubs brings the measured values closer to the calculated values in Fig. S4, and the open stubs was necessary for the equivalent circuit model.

The Au and graphene contacts of the CPW used in this study were represented by a parallel circuit of $R_{contact}$ and $C_{contact}$. Figure 8 shows the calculation and comparison of the impedance of $R_{contact}$ and $C_{contact}$ versus frequency. In the frequency range from 1 to 50 GHz, the impedance of $C_{contact}$ is clearly smaller, indicating that the contact impedance is dominated by capacitance¹⁰. Awan et al.'s study²⁹, which was used as a reference for constructing the equivalent circuit model, evaluated the transmission characteristic of CPW with SL graphene but did not assume that capacitance is the dominant factor in contact impedance. The value of $C_{contact}$ in Awan et al.'s experiment was set at 0.12 pF, which is smaller than our value ($C_{contact} > 200$ pF). This is because the contact area between the Au electrode and graphene in our study (Fig. 3a) is larger than in Awan et al. ($100 \mu\text{m}^2$). Thus, these results indicated that the large contact area between the Au and graphene enabled the $C_{contact}$ to be the dominant factor in the contact impedance.

Our research clarified the transmission characteristics of graphene for the 5G frequency by experimentally measuring the S_{21} of the CPW using the graphene at 1–50 GHz and comparing them with the constructed equivalent circuit model of the CPW. To our knowledge, our study is the first compare the S_{21} of various graphene materials with different electrical properties while maintaining transparency. From this comparison, we found that the graphene channel in the CPW can be expressed only in terms of resistance. In addition, multilayering and carrier doping are effective in reducing transmission loss of the graphene, and the contact impedance can be reduced by increasing the contact area between Au and graphene. These are important findings for the design of transparent 5G antenna devices using graphene.

It is evident that graphene will continue to be studied to lower resistivity, increase mobility, and enable processes for larger area, toward a variety of device applications. Our study is one step in that direction, and it has

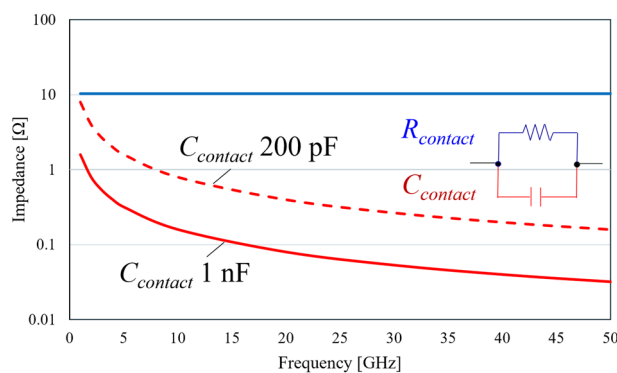


Figure 8. Calculated frequency dependence of impedance between graphene and Au electrode. $R_{contact}$ (10 Ω) of P-type doped 3L graphene (blue line), $C_{contact}$ (1 nF) of P-type doped 3L graphene (solid red line) and $C_{contact}$ (200 pF) of 3L graphene (dashed red line) from 1 to 50 GHz.

provided valuable insights not only for designing transparent 5G antennas with graphene but also for the design of other devices such as microwave ring resonators, absorber, photodetectors, and terahertz devices using the graphene.

Conclusion

We have fabricated CPWs using three types of graphene and measured the S_{21} from 1 to 50 GHz. We also measured the optical and electrical characteristics of the three types of graphene, built equivalent circuit models, and calculated. The agreement between the simulated S_{21} and measured S_{21} supports the validity of the constructed equivalent circuit model, in addition, the contact impedance value and the transmission loss of graphene channel were clarified. The comparison of the S_{21} of the three types of graphene shows that carrier doping and multilayering of graphene are effective in reducing transmission loss while maintaining the transparency of graphene in the operated 5G frequency. The results provide design guidelines for the introduction of graphene as a transparent conductive material in 5G antennas to replace existing materials such as meshed Cu, metal nanowires, and ITO films. Increasing the contact area between Au and graphene was also found to be effective in reducing contact impedance. In designing 5G antennas, it is important to connect the device to the power feed with minimal losses, and our experimental results show that a large contact area between the graphene and electrode is an important consideration as it reduces contact losses.

Our findings provide insights into the design of millimeter-wave devices using graphene and, furthermore, provide the basis for the application of graphene as a radiating element of transparent 5G antennas.

Methods

Figure 9 shows a series of processes from graphene growth to device fabrication.

CVD growth and graphene stacking. To grow graphene as a uniform monolayer, Cu foil was selected as a catalyst substrate. Before graphene growth, the Cu foil was annealed at 1000 °C for 30 min in H_2 (20 sccm) atmosphere for cleaning. Graphene was grown by low-pressure CVD on the Cu foil using H_2 and CH_4 gas. The CVD growth proceeded for 30 min under H_2 (20 sccm) and CH_4 (2 sccm) flows at 1000 °C. For transfer processes, PMMA (Aldrich, M.W. = 996,000) in an ethyl lactate solution (4 wt%) was spin-coated onto graphene as a supporting layer and cured at 180 °C for 1 min.

The PMMA was wiped off with acetone during spin-coating because it also spread around to the back side of Cu foil. In the CVD process, graphene grew on both sides of the Cu foil, causing subsequent Cu etching failure. Therefore, oxygen plasma treatment (O_2 :30 sccm, power: 20 W, time: 60 s) was performed on the opposite side of the Cu foil from the side where the PMMA film was formed to remove the unwanted graphene. Then the PMMA coated SL graphene sheet was obtained by etching the Cu foil. To form SL graphene on a substrate, the PMMA-coated SL graphene sheet (size: $10 \times 10 \text{ mm}^2$) was transferred onto a quartz substrate (size: $20 \times 20 \text{ mm}^2$, thickness: 1 mm), and the PMMA was removed by immersing it in an acetone for 12 h. The 3L graphene samples were obtained by a layer-by-layer process in which a PMMA-coated SL graphene sheet was repeatedly transferred to another graphene grown on a Cu foil sample. The rest of the process was the same as that for fabricating SL graphene: etching Cu, transferring to the quartz substrate, and removing PMMA to obtain the 3L graphene on the quartz sample.

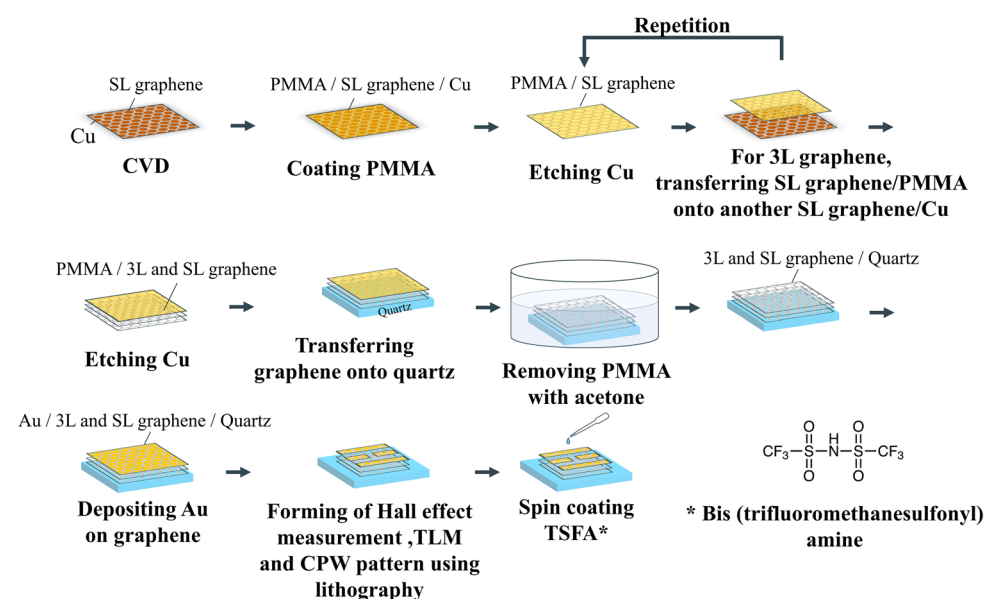


Figure 9. Graphene and device fabricating processes.

Device fabrication. For the device fabrication of TLM, Hall effect measurement, and the CPW, Au was deposited onto three types of graphene samples as electrode materials. The Au electrodes for the Hall effect measurement sample were deposited in vacuum using resistance heating at a rate of 1 Åm/s, and the resulting film thickness was 100 nm. In addition, for the TLM and CPW samples, Au electrodes were prepared by electron beam evaporation in vacuum at a rate of 10 Åm/s and deposited to a thickness of 500 nm.

Electrode patterning for each device formation was performed in two steps. The first process is to remove unwanted Au and graphene, and the second step is to remove Au on the graphene channel area. For the first process, a photo resist (Merck, AZ5214-E) was spin-coated onto the Au and cured at 90 °C for 1.5 min. After UV exposure, the samples were immersed in a developing solution (Merck, AZ 300MF DEVELOPER (2.38%)) to remove the resist from areas other than the electrode patterns. The samples were then immersed in Au etchant (Kanto Chemical, AURUM303) for 40 s to form the electrode pattern. Finally, the resist on the electrode pattern was removed using a remover (Merck, AZ remover 700), followed by oxygen plasma treatment (O₂:30 sccm, power:100 W, time : 120 s) to completely remove the resist and unwanted graphene residue. The second process is the formation of the graphene channel. Resist coating, UV exposure using a mask for channel formation, immersion in the developing solution, dipping in the Au etchant, followed by immersion in the developing solution again, and oxygen plasma treatment were performed as in the first process. Through these processes, various devices could be fabricated with graphene.

The P-type doped 3L graphene was obtained by dropping TFSA (TCI, B2541) in 1-butanol solution (50 mM) onto 3L graphene, allowing it to soak for 1 min at room temperature in air atmosphere, and then spin coating it¹⁰.

Data availability

The datasets analyzed in the current study are available from the corresponding authors upon request.

Received: 25 April 2023; Accepted: 18 August 2023

Published online: 24 August 2023

References

- Inomata, M. *et al.* Transparent glass antenna for 28GHz and its signal reception characteristics in urban environment. *14th European Conference on Antennas and Propagation*. 1–5 (2020).
- Nermeen, A. E. *et al.* Siler sandwiched ITO based transparent antenna array for RF energy harvesting in 5G mid-range of frequencies. *IEEE Access* **9**, 49476–49486 (2021).
- Yan, S., Wei, J. W. & Ting, T. H. A transparent SIW cavity-based millimeter-wave slot antenna for 5G communication. *IEEE Antennas Wirel. Propag. Lett.* **21**(6), 1105–1109 (2022).
- Kwok, K. S., Bao-jie, C. & Chi, C. H. C. Microwave and millimeter-wave MIMO antenna using conductive ITO film. *IEEE Access* **8**, 207024–207033 (2020).
- Chang, M. L., Youngsung, K., Yongjin, K., Li, K. K. & Chang, W. J. A flexible and transparent antenna on a polyimide substrate for laptop computers. *Microw. Opt. Technol. Lett.* **57**, 1038–1042 (2015).
- Junho, P. *et al.* An optically invisible antenna-on-display concept for millimeter-wave 5G cellular devices. *IEEE Trans. Antennas Propag.* **67**(5), 2942–2952 (2019).
- Darran, R. C. *et al.* Strain-dependent electrical resistance of tin-doped indium oxide on polymer substrates. *Appl. Phys. Lett.* **76**(11), 1425–1427 (2000).
- Gerald, O., Mark, W. & Craig, Z. Theoretical interpretation of Moiré patterns. *J. Opt. Soc. Am.* **54**(2), 169–175 (1964).
- Kosuga, S., Suga, R., Hashimoto, O. & Koh, S. Graphene-based optically transparent dipole antenna. *Appl. Phys. Lett.* **110**, 233102 (2017).
- Koh, S. *et al.* Graphene transparent antennas. *Carbon Rep.* **2**, 23–30 (2023).
- Murata, H. *et al.* High-electrical-conductivity multilayer graphene formed by layer exchange with controlled thickness and interlayer. *Sci. Rep.* **9**, 4068 (2019).
- Emre, O. P., Osman, B. & Coskun, K. Graphene based flexible electrochromic devices. *Sci. Rep.* **4**, 6484 (2014).
- Thomas, H. B. *et al.* Large-area functionalized CVD graphene for work function matched transparent electrodes. *Sci. Rep.* **5**, 16464 (2015).
- Ivan, K. *et al.* Novel highly conductive and transparent graphene-based conductors. *Adv. Mater.* **24**, 2844–2849 (2012).
- Pan, K. *et al.* Sustainable production of highly conductive multilayer graphene ink for wireless connectivity and IoT applications. *Nat. Commun.* **9**, 5197 (2018).
- Sadon, S. N. *et al.* Analysis of Graphene Antenna Properties for 5G Applications. *Sensor* **19**, 4835 (2019).
- Hong, S. K. *et al.* Electromagnetic interference shielding effectiveness of monolayer graphene. *Nanotechnology* **23**, 455704 (2012).
- Wang, Y., Tong, S. W., Xu, X. E., Özyilmaz, B. & Loh, K. P. Interface engineering of Layer-by-Layer stacked graphene anodes for high-performance organic solar cells. *Adv. Mater.* **23**, 1514 (2011).
- Moon, S. *et al.* Intrinsic high-frequency characteristics of graphene layers. *New J. Phys.* **12**, 113031 (2010).
- Grande, S. *et al.* Amplitude and phase modulation in microwave ring resonators by doped CVD graphene. *Nanotechnology* **29**, 325201 (2018).
- Otsuji, T. *et al.* Graphene-based devices in terahertz science and technology. *J. Phys. D. Appl. Phys.* **45**, 303001 (2012).
- Ryzhii, V., Otsuji, T. & Shur, M. Graphene based plasma-wave devices for terahertz applications. *Appl. Phys. Lett.* **116**, 140501 (2020).
- Somayyeh, A. & Tapio, F. Terahertz graphene-based multi-functional anisotropic metamaterial and its equivalent circuit model. *Sci. Rep.* **13**, 3433 (2023).
- Kosuga, S. *et al.* Optically transparent antenna based on carrier-doped three-layer stacked graphene. *AIP Advance*. **11**, 1–6 (2021).
- Mohapatra, A., Rao, M. S. R. & Jaiswal, M. Thermal transport in turbostratic multilayer graphene. *Carbon* **201**, 120–128 (2023).
- Donghyuk, K., Dongchan, D., Lee, Y. L. & Duk, Y. J. Work-function engineering of graphene anode by bis(trifluoromethanesulfonyl) amide doping for efficient polymer light-emitting diodes. *Adv. Funct. Mater.* **25**, 5049–5055 (2013).
- Ferrari, A. C., Meyer, J. C. & Scardaci, V. Raman spectrum of graphene and graphene layers. *Phys. Rev. Lett.* **97**, 187401 (2006).
- Kosuga, S., Suga, R., Watanabe, T., Hashimoto, O. & Koh, S. Characterization of contact properties at interface between metal and graphene up to 15GHz. *Eng. Rep.* **3**, 1–6 (2020).
- Awan, S. A. *et al.* Transport conductivity of graphene at RF and microwave frequencies. *2D Materials* **3**(1), 1–11 (2016).
- Mingguang, T. *et al.* Linear and nonlinear microwave characterization of CVD-grown graphene using CPW structure. In *9th European Conference on Antennas and Propagation*. 1–5 (2015).

31. Das, S. S., Shaffique, A., Hwang, E. H. & Enrico, R. Electronic transport in two-dimensional graphene. *Rev. Mod. Phys.* **83**, 407 (2011).
32. Wang, T., Hwang, E. H. & Das, S. S. Ballistic hot electron transport in graphene. *Phys. Lett.* **93**, 02318 (2008).
33. Alberto, M. *et al.* Thirty gigahertz optoelectronic mixing in chemical vapor deposited graphene. *Nano Lett.* **16**, 2988–2993 (2016).
34. Graef, H. *et al.* Ultra-long wavelength Dirac plasmons in graphene capacitors. *J. Phys. Mater.* **1**, 1–6 (2018).
35. Barannik, A. A. *et al.* Contactless exploration of graphene properties using millimeter wave response of WGM resonator. *Appl. Phys. Lett.* **113**, 094102 (2018).
36. Daniël, D. Z. & Luc, K. Skin effect modeling based on a differential surface admittance operator. *IEEE Trans. Microw. Theory Tech.* **53**(8), 2526–2538 (2005).
37. Uemura, K., Ikuta, T. & Maehashi, K. Turbostratic stacked CVD graphene for high-performance devices. *Jpn. J. Appl. Phys.* **57**, 030311 (2018).
38. Nagashio, K., Toriumi, A., Density-of-states limited contact resistance in graphene field-effect transistors. *Jpn. J. Appl. Phys.* **50**, 070108-1–6 (2011).
39. Nagashio, K., Nishimura, T., Kita, K. & Toriumi, A. Contact resistivity and current flow path at metal/graphene contact. *Appl. Phys. Lett.* **97**, 143514 (2010).
40. Dieter, K. S. Semiconductor material and device characterization. *Wiley IEEE press.* **3**, 127–184 (2005).
41. Uesugi, E., Goto, H., Eguchi, R., Fujiwara, A. & Kubozono, Y. Electric double-layer capacitance between an ionic liquid and few-layer graphene. *Sci. Rep.* **3**, 1595 (2013).
42. Cheng, Z., Justin, N., Jianzhong, W. & De-en, J. Quantum effects on the capacitance of graphene-based electrodes. *J. Phys. Chem. C* **119**, 22297–22303 (2015).
43. Dröscher, S. *et al.* Quantum capacitance and density of states of graphene. *Appl. Phys. Lett.* **96**, 152104 (2010).
44. Skulason, H. S. *et al.* Contactless impedance measurement of large-area high-quality graphene. In *2012 IEEE/MTT-S International Microwave Symposium Digest.* 12–17 (2012).

Acknowledgements

This work was partly supported by JSPS KAKENHI (Grant Nos. 19K05218, 20H02209, 23K04542 and 23H01470).

Author contributions

Experimental design, sample preparation, data collection: R.O., K.H., K.K. Data analysis: R.O., K.N. Wrote the paper: R.O. Supervision: R.S., T.W., S.K.

Competing interests

The authors declare no competing interests.

Additional information

Supplementary Information The online version contains supplementary material available at <https://doi.org/10.1038/s41598-023-40942-8>.

Correspondence and requests for materials should be addressed to R.O.

Reprints and permissions information is available at www.nature.com/reprints.

Publisher's note Springer Nature remains neutral with regard to jurisdictional claims in published maps and institutional affiliations.



Open Access This article is licensed under a Creative Commons Attribution 4.0 International License, which permits use, sharing, adaptation, distribution and reproduction in any medium or format, as long as you give appropriate credit to the original author(s) and the source, provide a link to the Creative Commons licence, and indicate if changes were made. The images or other third party material in this article are included in the article's Creative Commons licence, unless indicated otherwise in a credit line to the material. If material is not included in the article's Creative Commons licence and your intended use is not permitted by statutory regulation or exceeds the permitted use, you will need to obtain permission directly from the copyright holder. To view a copy of this licence, visit <http://creativecommons.org/licenses/by/4.0/>.

© The Author(s) 2023